*Article*

# Boosting Photovoltaic Efficiency in Double Quantum Well Intermediate Band-Solar Cells through Impurity Positioning

**Angel E. Obispo *, Cristofher Zuñiga Vargas and William C. Algoner**

Facultad de Ingeniería Eléctrica y de Potencia, Universidad Tecnológica del Perú, Lima 15306, Peru; crzuniga@utp.edu.pe (C.Z.V.); walgoner@utp.edu.pe (W.C.A.)
* Correspondence: aobispo@utp.edu.pe

**Abstract:** The photovoltaic conversion efficiency of a single-intermediate band solar cell that incorporates a double quantum well structure consisting of GaAs/InAs/GaAs/InAs/GaAs embedded in the intrinsic region of conventional p-i-n structure is analyzed. The width of the intermediate band and the solutions for the two lowest energy states has been determined by solving the two-impurities-related Schrodinger equation based on the Numerov method. The position of these impurities determines three distinct cases: the system in the absence of impurities (Case 1), impurities at the center of GaAs quantum barriers (Case 2), and impurities at the center of InAs quantum wells (Case 3). The photovoltaic conversion efficiency has been calculated as a function of the widths $L$ y $H$ of the quantum well structures. The obtained results indicate an improvement in efficiency under the specific conditions of these parameters.

**Keywords:** solar cell; intermediate band; quantum well; impurities; Schrödinger equation; conversion efficiency

**Citation:** Obispo, A.E.; Zuñiga Vargas, C.; Algoner, W.C. Boosting Photovoltaic Efficiency in Double Quantum Well Intermediate Band-Solar Cells through Impurity Positioning. *Energies* **2023**, *16*, 7722. https://doi.org/10.3390/en16237722

Academic Editor: Peter D. Lund

Received: 12 September 2023
Revised: 13 November 2023
Accepted: 17 November 2023
Published: 23 November 2023

**Copyright:** © 2023 by the authors. Licensee MDPI, Basel, Switzerland. This article is an open access article distributed under the terms and conditions of the Creative Commons Attribution (CC BY) license (https://creativecommons.org/licenses/by/4.0/).

## 1. Introduction

Over the past five decades, solar energy has emerged as a crucial activity in most developed nations, particularly in the electricity generation sector. Consequently, the rapid advancement of photovoltaic technology has occurred exponentially, primarily because of its environmentally friendly characteristics. This starkly contrasts with the widespread pollution resulting from the excessive utilization of fossil fuels. In light of this challenge, solar cells have emerged as a highly advanced and promising alternative. They possess many advantageous attributes such as sustainability, reduced production and maintenance expenses, and user-friendliness [1]. The process of generating electrical energy relies crucially on a remarkable phenomenon known as the photovoltaic effect [1,2]. In essence, this phenomenon pertains to the liberation of electrons within a semiconductor material, which is catalyzed by the absorption of photons derived from incident sunlight, ultimately resulting in the generation of an electric current. In conventional solar cells, which are primarily composed of simple p-n junctions formed of silicon semiconductor plates [3], the absorption of solar radiation is restricted to photons that fall within a specific range of wavelengths. Consequently, some of these photons are converted into heat, while the remainder are regrettably lost, resulting in an inefficient energy-conversion process [4]. Within the context of silicon solar cells, the photovoltaic conversion efficiency, which measures the proportion of electrical energy generated by the cell in relation to the incident solar energy, has reached approximately 30% in a study by [5]. Surpassing this efficiency threshold is a challenge for the advancement of future photovoltaic technologies, leading to the emergence of what is now known as emerging solar cells [6].

Emerging solar cells represent a promising technology with the potential to outperform their traditional silicon-based counterparts owing to their higher efficiencies, reduced production costs, and increased adaptability. Nevertheless, despite the high expectations

regarding the commercial viability of these solar cells, it is necessary to continue the research and development of advanced technologies in this field. This category includes perovskite solar cells [7,8], which have demonstrated conversion efficiencies greater than 25%; organic solar cells [9,10], which are lightweight, flexible, and easy to produce in large quantities; thin-film solar cells [11,12], which are extremely thin and can be fabricated in various shapes and sizes; and intermediate band solar cells [13], including quantum dot intermediate band solar cells (QD-IBSC) [14,15] and quantum well intermediate band solar cells (QW-IBSC) [16–18], all featuring unique structures that facilitate photon absorption across a range of energies, resulting in superior solar energy-to-electricity conversion efficiencies. These intermediate bands (IB) serve as an energy bridge between the conduction and valence bands, resulting in a reduced energy gap required for electron excitation and subsequent conversion into electrical current [14,19]. Luque and Marti demonstrated that intermediate band solar cells could achieve a maximum efficiency of 63.2% [20], which significantly exceeds the Shockley–Queisser limit of 43.5% [21]. Their discovery has ignited a surge of interest and investment in the research and development of this technology as it holds substantial promise for enhancing the efficiency of solar energy conversion while simultaneously reducing the production costs of solar cells.

In this study, we consider a single-intermediate band solar cell that incorporates a double quantum well structure consisting of GaAs/InAs/GaAs/InAs/GaAs embedded in the intrinsic region of the conventional p-i-n structure. The design of this QW-IBSC draws inspiration from several theoretical [17,18,22,23] and experimental [13,24,25] investigations that utilize multiple semiconductor layers within the intrinsic region of the solar cell to produce intermediate-band states between the conduction and valence bands. While increasing the number of quantum wells is expected to result in decreased efficiency due to the introduction of additional barriers, which could increase recombination rates, it is plausible to identify an equilibrium configuration where the optimal dimensions of the wells and barriers mitigate this efficiency decrease and even lead to potential efficiency improvements. Previous studies, as documented in [17,26], have explored these scenarios under unconcentrated light conditions. Nevertheless, as mentioned previously in [13], the true potential of intermediate-band solar cells is realized under highly concentrated light. Here, we evaluated the conversion efficiency of a double QW-IBSC under fully concentrated light by introducing two hydrogenic impurities symmetrically into the volume of the intrinsic region (see Figure 1). Prior research [18,27] highlighted the performance-enhancing effects of hydrogenic impurities, which introduce additional states through the hybridization of impurity states with the energy band states of the material. In this study, we employed a methodology that allows us to identify the optimal configurations in which these impurities lead to an increase in efficiency.

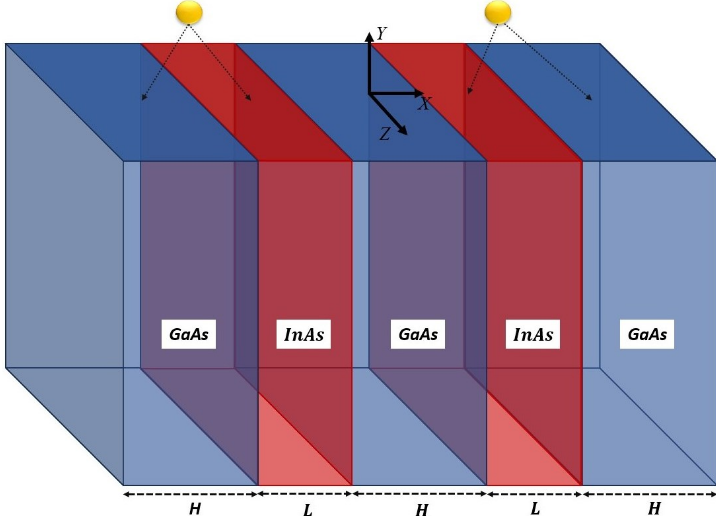


**Figure 1.** Schematic diagram of GaAs/InAs/GaAs/InAs/GaAs solar cells.

The organization of this paper is structured as follows: Section 2 outlines the theoretical framework. In Section 3, the results obtained from this study are analyzed and discussed. Finally, Section 4 concludes the paper.

## 2. Theoretical Considerations

To describe the dynamics of photoelectrons in a solar cell with an intermediate band, a cell model is used that incorporates two InAs semiconductor plates with width $L$, symmetrically embedded in a GaAs matrix along the [100] direction, as illustrated in Figure 1. The intermediate band is formed by additional states trapped in the quantum wells potentials generated by the presence of InAs. This type of cell is known as a quantum well intermediate band solar cell (QW-IBSC).

To numerically calculate the performance of solar cells, formally known as conversion efficiency ($\eta$), the following postulates must be satisfied:

- The solar cell must be thick and extensive enough to fully absorb all incident photons from the sun.
- Each photon that hits the solar cell can create only one electron–hole pair.
- Recombination must occur primarily through radiative transitions to achieve optimal conversion efficiency in the shortest possible time.
- Two of the three bands must exhibit photon absorption without overlap.
- The ohmic resistance of the device must be negligible.
- The solar cell should be considered as black body at a temperature of $T_c = 300$ K.
- The solar surface temperature was assumed to be $T_s = 6000$ K, whereas the room temperature was $T_r = T_c = 300$ K.

It is important to mention that according to theoretical [28,29] and experimental studies [14,19,30], thin films immersed in a semiconductor material can generate discrete energy levels for electron and hole states. In the scope of this investigation, a novel system is conceptualized wherein these states are effectively confined by the presence of a double quantum well composed of InAs. This configuration leads to the creation of an additional intermediate band, serving as a vital conduit connecting the conduction and valence bands (as illustrated in Figure 2). These quantum wells, each possessing a width denoted as $L$, are strategically positioned between three potential barriers with finite widths $H$. These barriers are associated with the GaAs matrix.

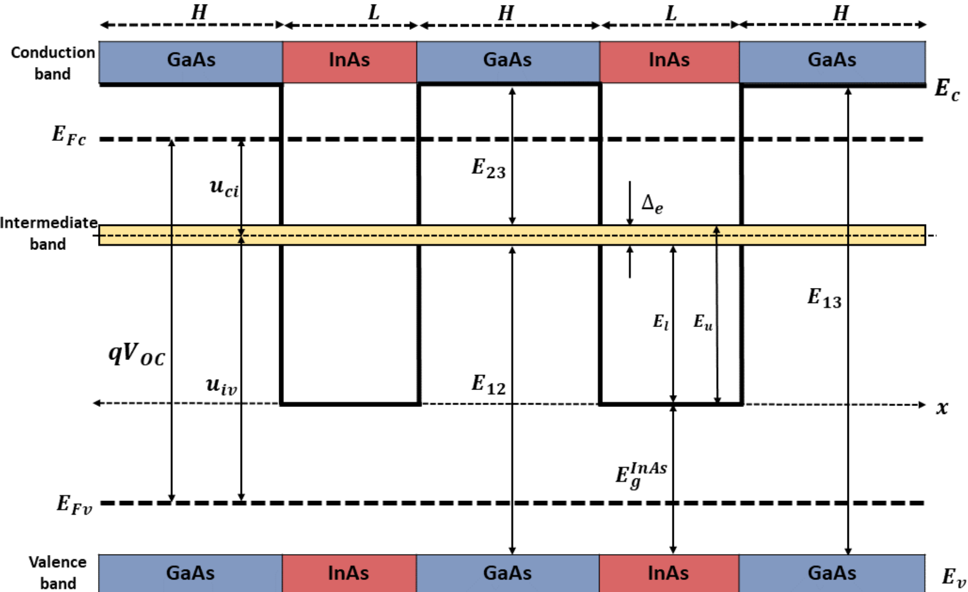


**Figure 2.** Energy diagram of the GaAs/InAs/GaAs/InAs/GaAs QW-IBSC along the [100] crystallographic direction.

### 2.1. Description of the Model

The dynamics of a single photoelectron associated with additional states in the intermediate band can be described by the Schrödinger equation $H\Psi = E\Psi$, where $\Psi$ represents the wave function and $E$ denotes the energy. Within this framework, the Hamiltonian, accounting for the effects of impurities, is defined as follows:

$$H = -\frac{\hbar^2}{2}\frac{d}{dx}\left(\frac{1}{m^*}\frac{d}{dx}\right) + v(x) - \frac{e^2}{4\pi\varepsilon_0\varepsilon|x-x_0|^2} - \frac{e^2}{4\pi\varepsilon_0\varepsilon|x+x_0|^2}, \quad (1)$$

where $\hbar$ is the reduced Planck constant; $m^*$ and $E$ are the effective mass and total energy of the electron, respectively; $e$ is the electron charge; $\varepsilon_0$ is the permittivity of the vacuum; $\varepsilon$ is the relative dielectric constant; and $x_0$ is the impurity position. Since the quantum wells associated with the GaAs/InAs/GaAs/InAs/GaAs junction rest in the [100] crystallographic direction, the effective potential $v(x)$ depends only on the coordinate $x$. The confinement adopted in this study corresponds to two finite square potential wells of width $L$. Formally,

$$v(x) = V_0\left[1 - \theta\left(x - \frac{H}{2}\right) - \theta\left(-x - \frac{H}{2}\right) + \theta\left(x - L - \frac{H}{2}\right) + \theta\left(-x - L - \frac{H}{2}\right)\right], \quad (2)$$

where $\theta(x)$ is the Heaviside function and $V_0$ is the conduction band offset corresponding with the depth of the InAs two quantum wells. According to Figure 2, this depth is proportional to the difference between the GaAs and InAs bandgap energies:

$$V_0 = g(E_g(GaAs) - E_g(InAs)) \quad (3)$$

where $g$ represents the band ratio, which for electrons is given by $g = 0.7$. On the other hand, we can also define the effective mass:

$$m^* = m_g^*(GaAs) + \left(m_g^*(GaAs) - m_g^*(InAs)\right)\times \left[\theta\left(x - L - \frac{H}{2}\right) + \theta\left(-x - L - \frac{H}{2}\right) - \theta\left(x - \frac{H}{2}\right) - \theta\left(-x - \frac{H}{2}\right)\right], \quad (4)$$

and the relative dielectric constant:

$$\varepsilon = \varepsilon_{GaAs} + (\varepsilon_{GaAs} - \varepsilon_{InAs})\times \left[\theta\left(x - L - \frac{H}{2}\right) + \theta\left(-x - L - \frac{H}{2}\right) - \theta\left(x - \frac{H}{2}\right) - \theta\left(-x - \frac{H}{2}\right)\right], \quad (5)$$

Unfortunately, this configuration does not allow for an exact form of the solutions to Equation (1), which requires the use of numerical calculation techniques. One of the commonly used numerical methods for solving the time-independent Schrödinger equation is the Numerov method, which discretizes the equation, decomposing it into discrete steps and making it computationally tractable. For this case, the discretized form of the Schrödinger equation is given by:

$$-\frac{\hbar^2}{2}\left(\frac{\Psi_{i+1} - 2\Psi_i + \Psi_{i-1}}{s^2}\right) = -\frac{1}{12}\left[(m^*V\Psi)_{i+1} + 10(m^*V\Psi)_i + (m^*V\Psi)_{i-1}\right] + \frac{E}{12}\left[(m^*\Psi)_{i+1} + 10(m^*\Psi)_i + (m^*\Psi)_{i-1}\right], \quad (6)$$

where $m_i^*$, $\Psi_i$, and $V_i$ denote the effective mass, the total potential, and the wave function at grid point $i$, respectively. Additionally, we considered a number of steps, $N$, calculated as $N = (x_{max} - x_{min})/s$, with $x_{max} = H + L$, $x_{min} = -H - L$, and a step value of $s = 0.01$ (nm).

### 2.2. Modelling of the Current Density and the Photovoltaic Conversion Efficiency

The short-circuit current density is directly proportional to the disparity between the photons absorbed by the device and those emitted from it. Here, we consider the spectral distribution dependence of the solar radiation, accounting for the energy content within each wavelength band. Building on the energy-band diagram illustrated in Figure 2, the short-circuit current density $J_{sc}$ of a QW-IBSC can be expressed as follows:

$$\frac{J_{sc}}{|e|} = [N(E_{13}, \infty, T_s, 0) - N(E_{13}, \infty, T_c, u_{CV})] + [N(E_{23}, E_{12}, T_s, 0) - N(E_{23}, E_{12}, T_c, u_{CI})], \quad (7)$$

where $u_{CV}$ and $u_{CI}$ are the chemical potentials related to the transitions between the valence band ($E_v$) and the conduction band ($E_c$) and between the conduction band and the intermediate band (BI), respectively. The first expression within the brackets in Equation (7) indicates the photon flux density produced in a conventional solar cell due to the direct transition of photo-electrons from the valence band to the conduction band. Conversely, the second expression between brackets denotes the density generated when electrons transition from the intermediate band to the conduction band. This photon flux $N(E_a, E_b, T, u)$ can be calculated using the Roosbroeck–Shockley formula [31]:

$$N(E_a, E_b, T, u) = \frac{2\pi}{h^3c^2} \int_{E_b}^{E_a} \frac{E^2 dE}{exp\left[\frac{E-u}{k_B T}\right] - 1}, \quad (8)$$

where $E_a$ and $E_b$ are the extremes of a absorption band, $u$ is the chemical potential, $c$ is the speed of light, and $k_B$ is the Boltzmann constant. Note that to determine the efficiency of this QW-IBSC, it is necessary to calculate each of the parameters in Equation (8). Next, we present a systematic methodology that allows us to determine each required parameter. From Figure 2, it is easy to identify the relations between the chemical potentials and the output voltage $V_{oc}$:

$$qV_{oc} = u_{CV} = u_{CI} + u_{IV}, \quad (9)$$

where $u_{CV}$ is the chemical potential associated with the transition between the valence and conduction bands. On the other hand, it is also possible to determine relations between the potentials $u_{CI}$ and $u_{IV}$ with the energies $E_{12}$ and $E_{23}$:

$$u_{CI} = E_{23} + 0.5\Delta_e - E_c + E_{FC}, \quad (10)$$

$$u_{IV} = E_{12} + 0.5\Delta_e - E_{FV} + E_v. \quad (11)$$

Here, $\Delta_e$ represents the width of the intermediate band, while $E_{FC}$ and $E_{FV}$ represent the energies of the Fermi quasi-levels in the conduction and valence bands, respectively. At the same time, these energies can be calculated using the following expressions:

$$E_c - E_{FC} = k_B T \cdot Ln\left(\frac{N_c}{n}\right), \quad (12)$$

$$E_{FV} - E_v = k_B T \cdot Ln\left(\frac{N_v}{p}\right), \quad (13)$$

where $N_c$ and $N_v$ are the densities of particles in the conduction and valence bands, respectively. The concentrations of electrons ($n$) and holes ($p$), as provided in [19], are expressed as:

$$n = N_c \cdot exp\left(-\frac{g\Delta_e}{k_B T_c}\right), \quad (14)$$

$$p = N_v \cdot exp\left(-\frac{(1-g)\Delta_e}{k_B T_c}\right). \quad (15)$$

Note that the values of $E_{13}$, $E_{12}$, and $E_{23}$ are required both in Equations (10) and (11) for the calculation of the effective potentials, as well as in the short-circuit current density $J_{sc}$ in Equation (7). From Figure 2, we have that:

$$E_{13} = E_{12} + E_{23} + \Delta_e, \quad (16)$$

where $E_{13}$ is the energy gap $E_g$ for the GaAs matrix. Additionally,

$$E_{12} = E_g(InAs) + E_l, \quad (17)$$

where $E_g(InAs)$ represents the gap of InAs (see Table 1) and $E_l$ is the lower boundary of the intermediate band (see Figure 2), which, together with the upper boundary $E_u$, allow one to determine the width of the intermediate band $\Delta_e$, as follows:

$$\Delta_e = E_u - E_l. \quad (18)$$

**Table 1.** Formulas used for the calculation of the electronic parameters.

| Electronic Parameter | Formula |
| --- | --- |
| Energy gap (GaAs) | $E_g(GaAs) = 1.424$ eV |
| Energy gap (InAs) | $E_g(InAs) = 0.354$ eV |
| Effective electron mass (GaAs) | $m^*(GaAs) = 0.067\ m_0$ |
| Effective electron mass (InAs) | $m^*(InAs) = 0.023\ m_0$ |
| Density of states in the conduction band (cm$^{-3}$) | $N_c(GaAs) = 4.45 \times 10^{17}$ |
| Density of states in the valence band (cm$^{-3}$) | $N_v(GaAs) = 8.87 \times 10^{18}$ |
| Relative dielectric constant (GaAs) | $\varepsilon_{GaAs} = 13.1$ |
| Relative dielectric constant (InAs) | $\varepsilon_{InAs} = 15.5$ |

As previously indicated, $E_u$ and $E_l$ will be numerically calculated by solving the Schrödinger Equation (1). Note that these energies start the calculation process that goes from Equation (18) to obtain the value of $J_{sc}$ in Equation (7).

In this particular scenario, the intensity of light on the QW-IBSC is determined by the number of suns, with one sun (or solar concentration factor $f_s = 1$) representing the standard radiation (un-concentrated light) at the surface of the Earth's atmosphere. Accordingly, the incident power density on the QW-IBSC is $P_{in} = f_s n_s \sigma T_s^4 = 1587.2\ \mathrm{W/m^2}$, where $\sigma$ represents the Stefan–Boltzmann constant and $n_s = 2.16 \times 10^{-5}$ is a geometric factor. On the other hand, fully concentrated light can theoretically be achieved when $f_s = 1/n_s = 46,296$. Here, we investigate the QW-IBSC efficiencies with fully concentrated light $f_s \times n_s = 1$ [32].

Finally, the fill factor $FF$ can be calculated as a function of both the voltage and temperature of the cell [33,34]:

$$FF = \frac{\frac{qV_{oc}}{k_B T} - ln\left(\frac{qV_{oc}}{k_B T} + 0.72\right)}{1 + \frac{qV_{oc}}{k_B T}}. \quad (19)$$

Thus, we obtain the efficiency of photovoltaic energy conversion for a QW-IBSC as follows:

$$\eta = \frac{V_{oc} \cdot J_{sc} \cdot FF}{P_{in}} = \frac{V_{oc} \cdot J_{sc} \cdot FF}{f_s \cdot 1587.2}. \quad (20)$$

## 3. Results and Discussions

The results shown in this section were obtained considering the values of the parameters summarized in Table 1. As mentioned earlier, the width of the intermediate band and its boundaries were numerically calculated. To assess the influence of hydrogen impurities, we systematically investigated three distinct scenarios:

- Case 1: QW-BISC without impurities (only $v(x)$ in Equation (1)).
- Case 2: Impurities located at the center of GaAs quantum barriers, $x_0 = \pm(L + H)$.
- Case 3: Impurities located at the center of InAs quantum wells, $x_0 = \pm(L + H)/2$.

Figure 3 illustrates the IB profile as a function of the size of the InAs quantum well (panel (a)) and width of the GaAs quantum barrier (panel (b)) for the three cases mentioned earlier. In general, the IB width in both panels tends to decrease in each case, with the system containing impurities in the center of the quantum wells (Case 3) displaying a notably wider IB (at small values of $L$ and $H$) compared to Cases 1 and 2. However, as $L$ and $H$ increase, this difference diminishes, as shown in panels (a) and (b), respectively. Note that the values obtained for the IB (intermediate band) in the QW-IBSC with impurities positioned at the center of the quantum barriers (Case 2) are slightly lower than those found in the case without impurities (Case 1), considering any $L$ and $H$ (see Figure 3). We believe that this behavior is due to the repulsive nature of the barriers, which might promote an environment conducive to increased charge carrier recombination in the presence of impurities. This would counteract any significant impact of impurities on the width of the IB and, consequently, on its performance. This behavior has already been reported in experimental scenarios in solar cells [24,35]. Case 3, on the other hand, represents a potential scenario in which the efficiency surpasses that reported in traditional GaAs p-i-n cells.

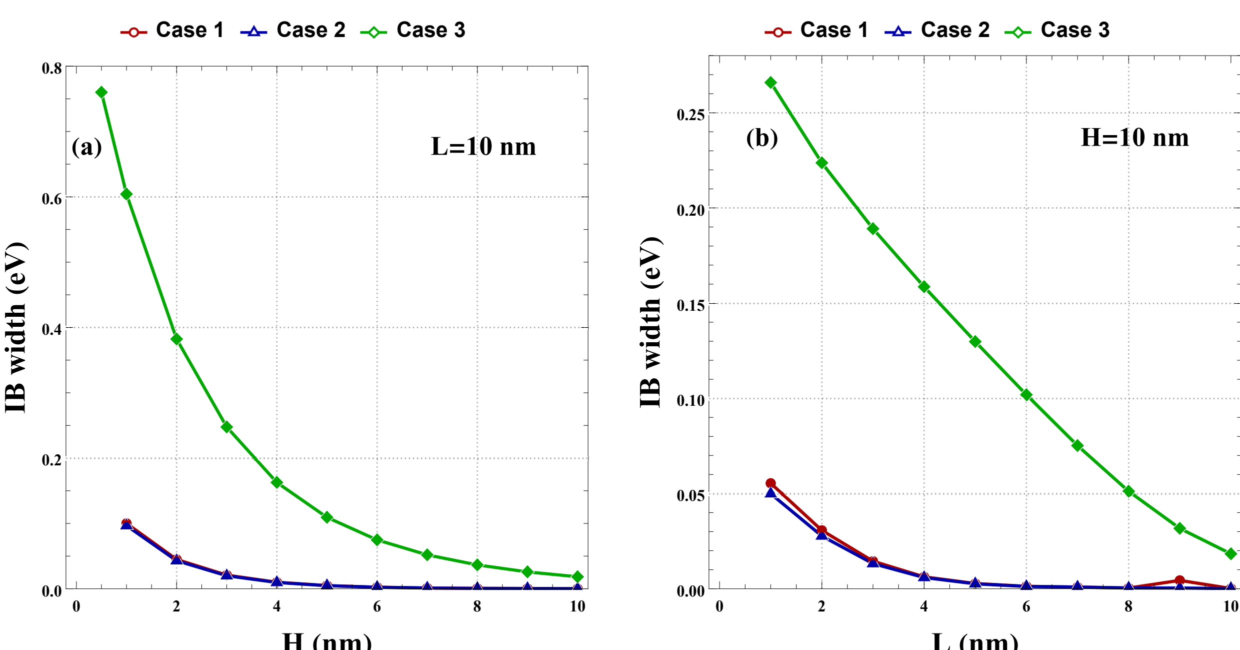


**Figure 3.** Profile of the width of intermediate bandgap $\Delta_e$: (**a**) as a function of $H$; (**b**) as a function of $L$.

Figure 4 shows the J-V characteristic profile of the proposed QW-IBSC under fully concentrated light for Cases 1 (red line), 2 (blue line), and 3 (green line), where the short-circuit current density is normalized by the power factor ($J_{sc}/f_s$); meanwhile, the open circuit voltage ($V_{oc}$) is approximately constant. Note that the position of impurities directly influences normalized current density. The QW-IBSC containing impurities in the center of the quantum wells (Case 3) denotes a higher $J_{sc}$ value than in other cases. This behavior

results from the enhanced photon absorption and electron excitation within the solar cell, leading to an increased photogenerated current. These results are consistent with those shown in Figure 3.

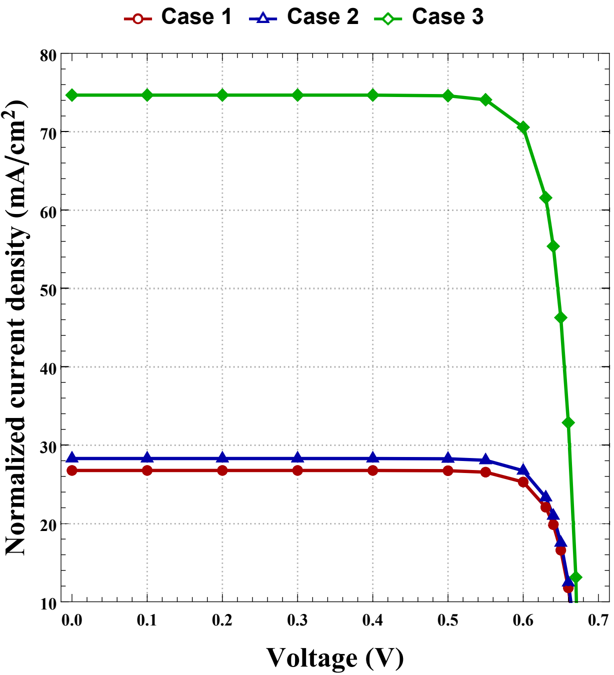


**Figure 4.** J-V characteristic curve of the QW-IBSC under fully concentrated light.

It is important to highlight that the effects of impurities on the localized states in the IB can also be determined using the Anderson model, as reported in [36,37]. Nevertheless, for the specific goals of this study, where the calculation of energies $E_u$ and $E_l$ is crucial, the Schrödinger equation emerges as a robust alternative to the Anderson model, even in the presence of impurities. In this framework, we show that the presence of both impurities leads to reordering in the distribution of localized states in the system because they influence the additional photoelectron states responsible for generating the IB. To illustrate this reordering, we examine the behavior of the local density of the ground state $\mid \Psi_{gs} \mid^2$ as a function of x [38]. This local density is numerically calculated from the normalized solution of Equation (1), corresponding to the lower energy limit $E_u$ of the IB, with $L = 10$ nm and specific values of $H$, which are 3, 5, 7, and 9 nm. In the context of Figure 5 (Case 2), brighter regions indicate a high probability of locating electrons, which occurs for $H \leq 5$ nm in regions close to the position of the InAs quantum wells (panels (a) and (b)). Nevertheless, when the width of the barrier $H$ increases (panels (c) and (d)), the intensity of the local density diminishes nonuniformly throughout the intrinsic region of the cell. Note that the presence of impurities induces the system to distribute states asymmetrically. Additionally, note that there is a natural tendency for the states to cluster near one impurity or another, indicating that there will be a region of the cell with different performances to the other.

In Figure 6, similar behavior is observed, considering a fixed value of $H = 10$ nm and varying $L$. In this configuration, the states were predominantly concentrated on one side of the intrinsic region as the size of the quantum well increased. This implies that there are configurations in which half of the cells behave differently than the other half. However, it is important to note that having regions of the cell with differentiated performance does not lead to optimal efficiency as it is assumed that solar light uniformly impinges on the entire cell; thus, less efficient regions would waste solar energy.

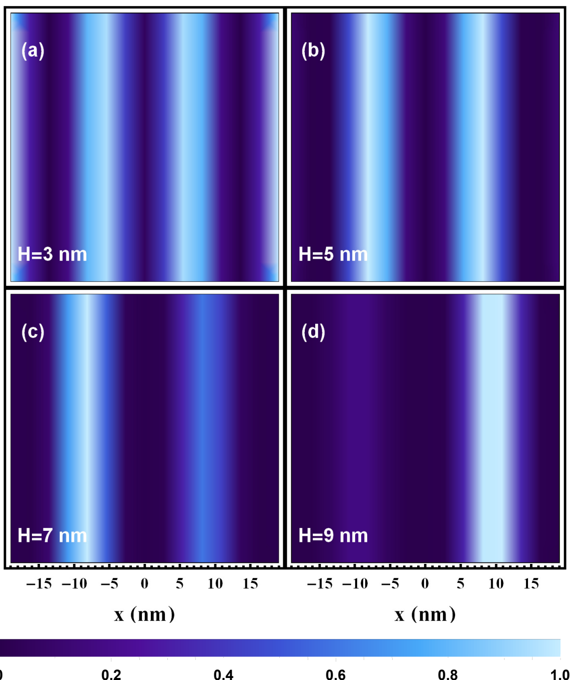


**Figure 5.** Local density of the ground state (units of 1/nm) as a function of x, for Case 2: (**a**) $H = 3$ nm; (**b**) $H = 5$ nm; (**c**) $H = 7$ nm; and (**d**) $H = 9$ nm.

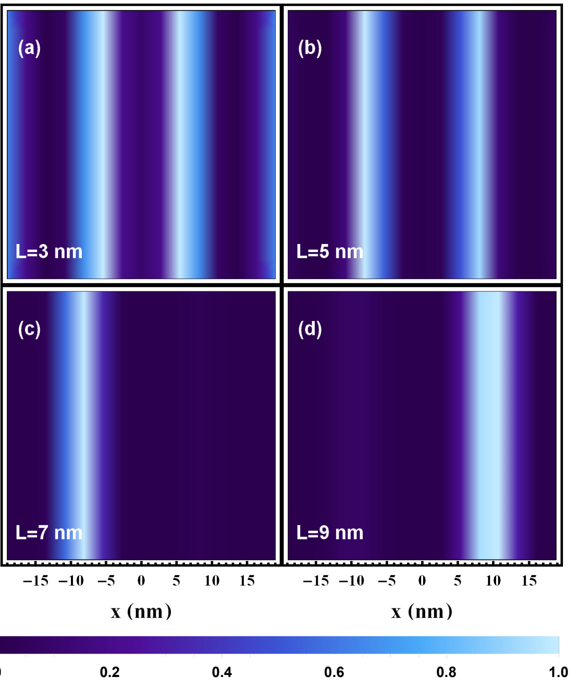


**Figure 6.** Local density of the ground state (units of 1/nm) as a function of x, for Case 2: (**a**) $L = 3$ nm; (**b**) $L = 5$ nm; (**c**) $L = 7$ nm; and (**d**) $L = 9$ nm.

Figure 7 shows the behavior of the local density of the ground state in the context of Case 3, considering a constant value of $L = 10$ nm and varying $H$ at 3, 5, 7, and 9 nm. The local density exhibits two peaks of maximum intensity symmetrically located and opposite to the axis of the central barrier when impurities are situated in the center of the quantum wells. Note that the areas of maximum density tend to separate as $H$ increases (panels (a)–(d)). However, owing to the confinement exerted by quantum wells, these additional states remain restricted between the impurity positions. Unlike in Figures 5 and 6, in this

configuration the local density displays symmetry in both cell halves, indicating uniform behavior. However, in Figure 8, considering $H = 10$ nm, the formation of a single peak of maximum density in the regions near the midpoint of the central barrier is observed. Nevertheless, this peak splits into two uniform and symmetrical peaks as the size of the quantum well $L$ increases (panels (a)–(d)). Therefore, based on these configurations, it could be argued that cells with impurities located in the center of the quantum wells would offer improved performance compared to Cases 1 and 2.

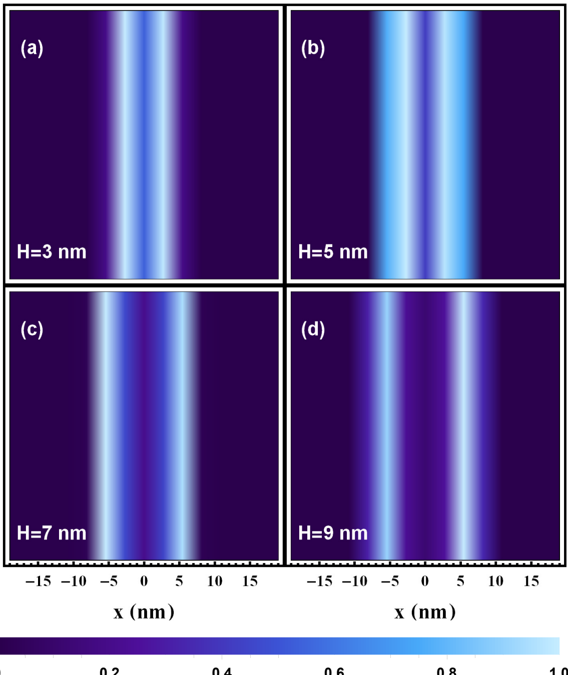


**Figure 7.** Local density of the ground state (units of 1/nm) as a function of x, for Case 3: (**a**) $H = 3$ nm; (**b**) $H = 5$ nm; (**c**) $H = 7$ nm; and (**d**) $H = 9$ nm.

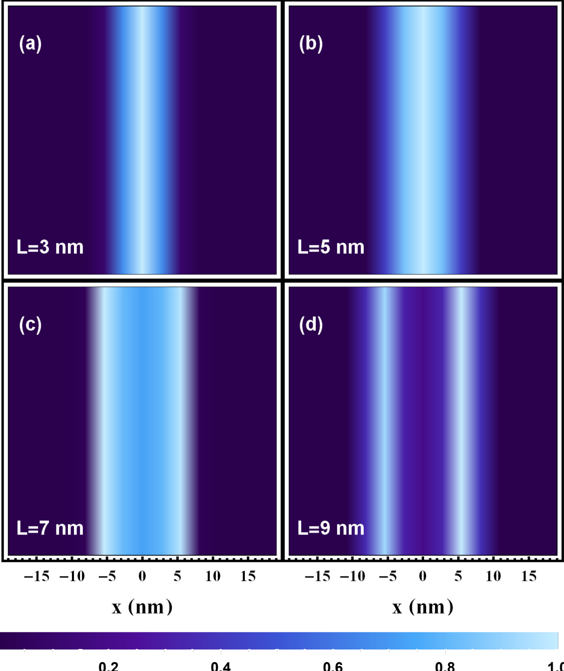


**Figure 8.** Local density of the ground state (units of 1/nm) as a function of x, for Case 3: (**a**) $L = 3$ nm; (**b**) $L = 5$ nm; (**c**) $L = 7$ nm; and (**d**) $L = 9$ nm.

Finally, following a detailed study and analysis of the quantum behavior of the parameters that determine the cell performance, it is necessary to address the most critical parameter for a QW-IBSC. Figure 9 shows the photovoltaic conversion efficiency ($\eta$) as a function of $H$ for the three cases analyzed above. Here, the value of $L$ is fixed at 10 nm, with an estimated value of $FF$ approximately equal to 0.84 based on Equation (19). Note that the curves for Case 3 increase slowly with $H$, reaching the maximum efficiency peak for $H \approx 2.0$ nm, which is approximately 28%. In contrast, the efficiency profiles for both Case 1 and Case 2 exhibit a slow decrease from 11% and 10%, respectively, at $H = 1$ nm. Notably, in all cases, for sufficiently large values of $H$, the efficiency tends toward a constant value, with Case 3 stabilizing at approximately 27%, whereas Cases 1 and 2 stabilize at 10.1% and 9.8%, respectively. We attribute this phenomenon to the synergy between the intermediate band, enabling the increased absorption of low-energy photons and the generation of additional charge carriers, counteracting the potential efficiency reductions caused by an increase in the GaAs barrier width, in conjunction with the appropriate cell width that minimizes the recombination rate, as documented in [17,26]. While these findings suggest that the inclusion of impurities at the InAs quantum well centers (Case 1) results in improved efficiency compared with the absence of impurities (Case 2), it is important to note that the configurations depicted in Figure 9 do not necessarily represent the most favorable scenarios.

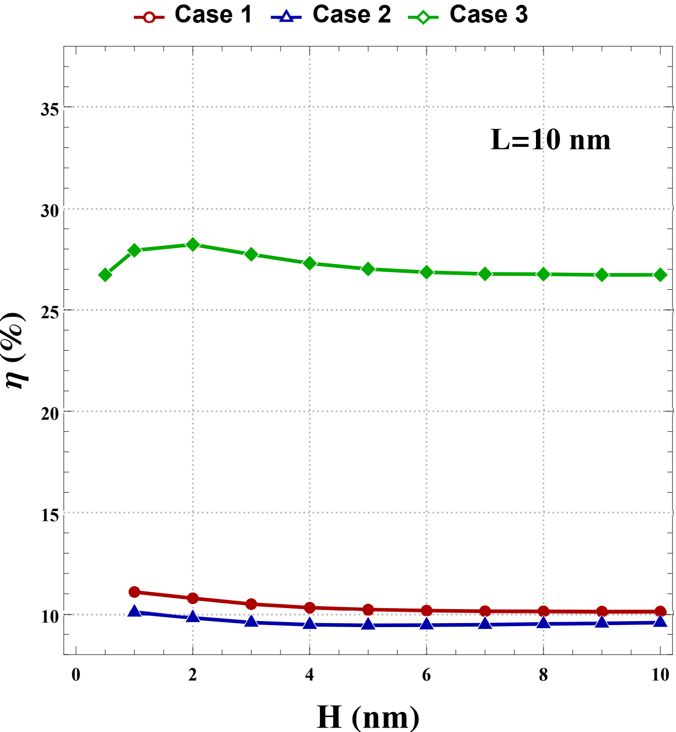


**Figure 9.** Photovoltaic conversion efficiency as a function of the $H$ for Cases 1, 2, and 3.

Figure 10 presents the photovoltaic conversion efficiency profile ($\eta$) as a function of $L$ while maintaining a fixed value of $H$ at 10 nm. The conversion efficiency decreased in all cases. Notably, the efficiency profile of Case 3 remains preeminent compared with the curves of Cases 1 and 2, which possess similar characteristics. Although no efficiency peaks are observed in this scenario, it is plausible to assert that the photovoltaic conversion efficiency attains its highest value for small values of $L$, surpassing the values shown in Figure 9 for each case. Specifically, the conversion efficiencies for cases 1 and 2 reach maximum values of 32.5% and 31.5%, respectively, at $L = 1$ nm. These results confirm that the presence of impurities at the center of the barriers (Case 2) does not significantly modify the performance of the impurity-free QW-IBSC (Case 1). However, their efficiencies rapidly approached the values achieved in Case 3 when $L$ decreased, where the QW-IBSC attained

a maximum efficiency of approximately 36% at $L = 1$ nm. It is important to mention that considering that highly concentrated light sets the ideal scenario in which both the QD-IBSC and QW-IBSC demonstrate high efficiency, as explained in [13]. It is possible to verify that the ratio between the maximum efficiency under fully concentrated light, which was found to be 36% in this study, and the efficiency obtained using unconcentrated light, which was 9.2% in the absence of impurities under the same conditions [17], is approximately two to one. This result is significantly greater than what has been observed in similar contexts [39–42].

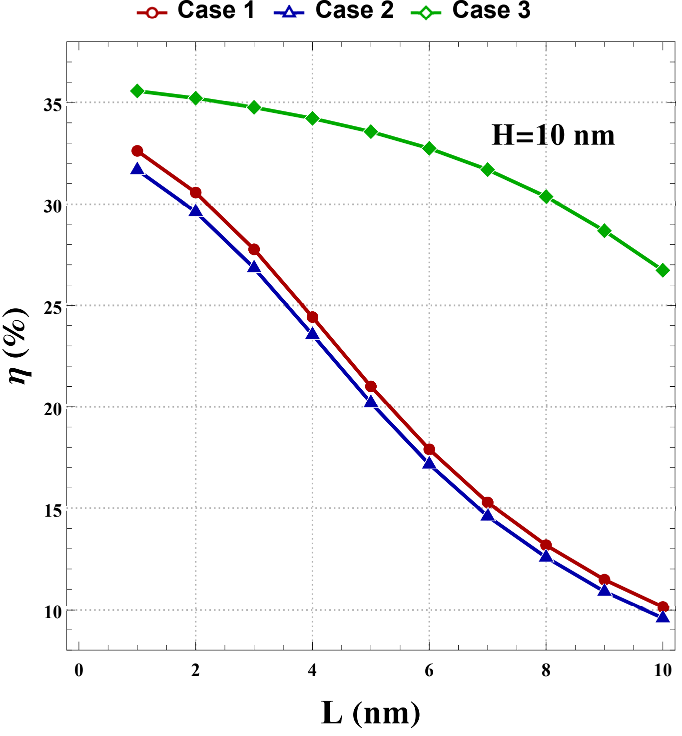


**Figure 10.** Photovoltaic conversion efficiency as a function of the $L$ for Cases 1, 2, and 3.

It is crucial to elucidate that the placement of impurities outside the central regions of the side barriers or wells leads to diminished efficiencies compared to the results presented in this study. These findings have been consistently validated through simulations employing the same parameters as those outlined in this study, thereby emphasizing the fundamental role of central impurity placement in achieving the highest efficiencies, as elucidated in this study. The case of impurities placed at the center of the central barrier has already been analyzed for a cell with a similar structure in reference [18].

## 4. Conclusions

We performed a theoretical investigation to explore the potential improvement in the performance of a GaAs/InAs/GaAs/InAs/GaAs double QW-IBSC. This architecture was inspired by various prior theoretical [17,18,23] and experimental [13,24,25] studies, which used multiple semiconductor layers in the intrinsic region of the cell, thereby generating intermediate-band states between the conduction and valence bands. We investigated the effects of changes in the impurity positions on these intermediate band states and determined how these changes modified the conversion efficiency.

Within the parameters of our model, the conversion efficiency was mathematically calculated through the solution of the two-impurity-related Schrödinger equation in three distinct cases. The lowest energy states and boundaries of the intermediate band produced by InAs and their corresponding wavefunctions were numerically calculated using the Numerov method. Figure 3a,b demonstrate that the intermediate bandwidth decreases exponentially as the width of the barrier, H, and the width of the quantum well, L, increase.

However, in Case 3 (impurities centered in the InAs quantum wells), a notable increase in the bandwidth was observed for small values of both $H$ and $L$. In Figure 4, the J-V characteristic profile also displays the predominant behavior of Case 3 compared with the other cases. However, the analysis of the local density of the ground state enabled us to discern the differences observed in the previous cases in terms of the localization of states associated with impurities. The configurations that produced the highest performance were those that exhibited local density with bright regions symmetrically positioned about the central barrier. Concerning the conversion efficiency, Case 3 displayed a progressive improvement in efficiency with increasing $H$, reaching a peak of approximately 28% at $H \approx 2.0$ nm. Cases 1 and 2 confirmed the presence of central impurities with minimal impact on cell performance. All cases exhibit efficiency stabilization for large $H$ values of approximately 10.1%, 9.8%, and 27% for Cases 1, 2, and 3, respectively. Finally, in Figure 10, the conversion efficiencies for cases 1 and 2 reach maximum values of 32.5% and 31.5%, respectively, at $L = 1$ nm. Additionally, Case 3 achieved a maximum efficiency of approximately 36%.

It is essential to clarify that when impurities are placed within side barriers or wells, except at the center, the efficiencies are lower than those presented in this study. These findings have been consistently verified in simulations using the same parameters as those presented in this study, underscoring the significance of central impurity placement in achieving the highest efficiencies, as shown in this study.

**Author Contributions:** Conceptualization, A.E.O.; formal analysis and investigation, A.E.O., C.Z.V. and W.C.A.; writing—original draft preparation, A.E.O.; Methodology, A.E.O., C.Z.V. and W.C.A.; writing—review and editing, C.Z.V. and W.C.A. All authors have read and agreed to the published version of the manuscript.

**Funding:** This research was funded by Universidad Tecnológica del Perú (UTP).

**Data Availability Statement:** The data presented in this study are available on request from the corresponding author.

**Conflicts of Interest:** The authors declare no conflict of interest.

## References

1. Singh, G.K. Solar power generation by PV (photovoltaic) technology: A review. *Energy* **2013**, *53*, 1–13 [CrossRef]
2. Rappaport, P. The photovoltaic effect and its utilization. *Sol. Energy* **1959**, *3*, 8–18. [CrossRef]
3. Wenham, S.R.; Green, M.A. Silicon solar cells. *Prog. Photovoltaics Res. Appl.* **1996**, *4*, 3–33. [CrossRef]
4. Sun, Z.; Chen, X.; He, Y.; Li, J.; Wang, J.; Yan, H.; Zhang, Y. Toward Efficiency Limits of Crystalline Silicon Solar Cells: Recent Progress in High-Efficiency Silicon Heterojunction Solar Cells. *Adv. Energy Mater.* **2022**, *12*, 2200015. [CrossRef]
5. Emery, K.A.; Osterwald, C.R. Solar cell efficiency measurements. *Sol. Cells* **1986**, *17*, 253–274. [CrossRef]
6. Almora, O.; Baran, D.; Bazan, G.C.; Cabrera, C.I.; Erten-Ela, S.; Forberich, K.; Guo, F.; Hauch, J.; Ho-Baillie, A.W.Y.; Jacobsson, T.J.; et al. Device Performance of Emerging Photovoltaic Materials (Version 3). *Adv. Energy Mater.* **2023**, *13*, 2203313. [CrossRef]
7. Wu, T.; Qin, Z.; Wang, Y.; Wu, Y.; Chen, W.; Zhang, S.; Cai, M.; Dai, S.; Zhang, J.; Liu, J.; et al. The main progress of perovskite solar cells in 2020–2021. *Nano-Micro Lett.* **2021**, *13*, 1–18. [CrossRef]
8. Kumar, N.S.; Naidu, K.C.B. A review on perovskite solar cells (PSCs), materials and applications. *J. Materiomics* **2021**, *7*, 940–956. [CrossRef]
9. Fukuda, K.; Yu, K.; Someya, T. The Future of Flexible Organic Solar Cells. *Adv. Energy Mater.* **2020**, *10*, 2000765. [CrossRef]
10. Hu, Z.; Wang, J.; Ma, X.; Gao, J.; Xu, C.; Yang, K.; Wang, Z.; Zhang, J.; Zhang, F. A critical review on semitransparent organic solar cells. *Nano Energy* **2020**, *78*, 105376. [CrossRef]
11. Mavlonov, A.; Razykov, T.; Raziq, F.; Gan, J.; Chantana, J.; Kawano, Y.; Nishimura, T.; Wei, H.; Zakutayev, A.; Minemoto, T.; et al. A review of Sb2Se3 photovoltaic absorber materials and thin-film solar cells. *Sol. Energy* **2020**, *201*, 227–246. [CrossRef]
12. Romeo, A.; Artegiani, E. CdTe-based thin film solar cells: Past, present and future. *Energies* **2021**, *14*, 1684. [CrossRef]
13. Okada, Y.; Ekins-Daukes, N.J.; Kita, T.; Tamaki, R.; Yoshida, M.; Pusch, A.; Hess, O.; Phillips, C.C.; Farrell, D.J.; Ahsan, N.; et al. Intermediate band solar cells: Recent progress and future directions. *Appl. Phys. Rev.* **2015**, *2*, 021302. [CrossRef]
14. Albaladejo-Siguan, M.; Baird, E.C.; Becker-Koch, D.; Li, Y.; Rogach, A.L.; Vaynzof, Y. Stability of Quantum Dot Solar Cells: A Matter of (Life)Time. *Adv. Energy Mater.* **2021**, *11*, 2003457. [CrossRef]
15. Beattie, N.S.; See, P.; Zoppi, G.; Ushasree, P.M.; Duchamp, M.; Farrer, I.; Ritchie, D.A.; Tomić, S. Quantum Engineering of InAs/GaAs Quantum Dot Based Intermediate Band Solar Cells. *ACS Photonics* **2017**, *4*, 2745–2750. [CrossRef]

16. Sayed, I.; Bedair, S.M. Quantum Well Solar Cells: Principles, Recent Progress, and Potential. *IEEE J. Photovoltaics* **2019**, *9*, 402–423. [CrossRef]
17. Madani, L. Numerical Simulation of InAs/GaAs Quantum well and Quantum Dots Solar Cells. Master Dissertation, University of Biskra, Biskra, Algeria, 2019.
18. El Ghazi, H. Numerical investigation of one-intermediate band InN/GaN QW solar cell under electric field, impurity and size effects. *Phys. B Condens. Matter.* **2020**, *602*, 412427. [CrossRef]
19. Cho, E.-C.; Park, S.; Hao, X.; Song, D.; Conibeer, G.; Park, S.-C.; Green, A.M. Silicon quantum dot/crystalline silicon solar cells. *Nanotechnology* **2008**, *19*, 245201. [CrossRef]
20. Luque, A.; Martí, A. Increasing the Efficiency of Ideal Solar Cells by Photon Induced Transitions at Intermediate Levels. *Phys. Rev. Lett.* **1997**, *78*, 5014–5017. [CrossRef]
21. Wiemer, M.; Sabnis, V.; Yuen, H. 43.5% efficient lattice matched solar cells. In Proceedings of the SPIE 8108, High and Low Concentrator Systems for Solar Electric Applications, San Diego, CA, USA, 21–25 August 2011; Volume VI, pp. 810804–810805.
22. Mishra, S.; Satpathy, S. One-dimensional photonic crystal: The Kronig-Penney model. *Phys. Rev. B* **2003**, *68*, 045121. [CrossRef]
23. Abbasian, S.; Sabbaghi-Nadooshan, R. Study of hole-blocking and electron-blocking layers in a InaS/GaAs multiple quantum-well solar cell. *Electron. Energetics* **2020**, *33*, 477–487. [CrossRef]
24. Ahn, K.; Kim, S.Y.; Kim, S.; Son, D.H.; Kim, S.H.; Kim, S.; Kim, J.; Sung, S.J.; Kim, D.H.; Kang, J.K. Flexible high-efficiency CZTSSe solar cells on stainless steel substrates. *J. Mater. Chem. A* **2019**, *7*, 24891–24899. [CrossRef]
25. France, R.M.; Geisz, J.F.; Song, T.; Olavarria, W.; Young, M.; Kibbler, A.; Steiner, M.A. Triple-junction solar cells with 39.5% terrestrial and 34.2% space efficiency enabled by thick quantum well superlattices. *Joule* **2022**, *6*, 1121–1135. [CrossRef]
26. Talhi, A.; Belghachi, A.; Moughli, H.; Amiri, B.; Varani, L. Numerical simulation of multi-quantum well solar cells GaAs/InAs using silvaco atlas. *Dig. J. Nanomater. Biostruct.* **2016**, *11*, 1361–1366.
27. Abboudi, H.; El Ghazi, H.; Jorio, A.; Zorkani, I. Impurity-related photovoltaic efficiency of (In,Ga)N/GaN quantum well-single intermediate band solar cell considering heavy hole impact. *Superlattices Microstruct.* **2021**, *150*, 106756. [CrossRef]
28. Paxman, M.; Nelson, J.; Braun, B.; Connolly, J.; Barnham, K.W.J.; Foxon, C.T.; Roberts, J.S. Modeling the spectral response of the quantum well solar cell. *J. Appl. Phys.* **1993**, *74*, 614–621. [CrossRef]
29. Anderson, N.G. Ideal theory of quantum well solar cells. *J. Appl. Phys.* **1995**, *78*, 1850–1861. [CrossRef]
30. Vadiee, E.; Fischer, A.M.; Clinton, E.A.; McFavilen, H.; Patadia, A.; Arena, C.; Ponce, F.A.; King, R.R.; Honsberg, C.B.; Doolittle, W.A. Evaluating the performance of InGaN/GaN multi-quantum-well solar cells operated at elevated temperatures via DC and small-signal AC analysis. *Jpn. J. Appl. Phys.* **2019**, *58*, 101003. [CrossRef]
31. Parrott, J. Radiative recombination and photon recycling in photovoltaic solar cells. *Sol. Energy Mater. Sol. Cells* **1993**, *30*, 221–231. [CrossRef]
32. Aly, A.E.-M.M.; Nasr, A. Theoretical performance of solar cell based on mini-bands quantum dots. *J. Appl. Phys.* **2014**, *115*, 114311. [CrossRef]
33. Green, M.A. *Solar Cells: Operating Principles Technology and System Applications*; Prentice-Hall: Englewood Cliffs, NJ, USA, 1982; p. 80.
34. Díaz, S.R. A generalized theoretical approach for solar cells fill factors by using Shockley diode model and Lambert W-function: A review comparing theory and experimental data. *Physica B* **2021**, *624*, 413427. [CrossRef]
35. Xie, W.; Yan, Q.; Sun, Q.; Li, Y.; Zhang, C.; Deng, H.; Cheng, S. A Progress Review on Challenges and Strategies of Flexible $Cu_2ZnSn(S,Se)_4$ Solar Cells. *Solar RRL* **2023**, *7*, 2201036. [CrossRef]
36. Zhang, Y.; Nelson, R.; Tam, K.-M.; Ku, W.; Yu, U.; Vidhyadhiraja, N.S.; Terletska, H.; Moreno, J.; Jarrell, M.; Berlijn, T. Origin of localization in Ti-doped Si. *Phys. Rev. B* **2018**, *98*, 174204. [CrossRef]
37. Malerba, C.; Ricardo, C.L.A.; D'Incau, M.; Biccari, F.; Scardi, P.; Mittiga, A. Nitrogen doped $Cu_2O$: A possible material for intermediate band solar cells? *Sol. Energy Mater. Sol. Cells* **2012**, *105*, 192–195. [CrossRef]
38. Laroze, D.; Barseghyan, M.; Radu, A.; Kirakosyan, A. Laser driven impurity states in two-dimensional quantum dots and quantum rings. *Physica B* **2016**, *501*, 1–4. [CrossRef]
39. Aly, A.E.-M.; Nasr, A. Theoretical Study of One-Intermediate Band Quantum Dot Solar Cell. *Int. J. Photoenergy* **2014**, *2014*, 1–10. [CrossRef]
40. Tomić, S.; Sogabe, T.; Okada, Y. In-plane coupling effect on absorption coefficients of InAs/GaAs quantum dots arrays for intermediate band solar cell. *Prog. Photovoltaics Res. Appl.* **2014**, *23*, 546–558. [CrossRef]
41. Imran, A.; Jiang, J.; Eric, D.; Yousaf, M. Numerical modelling of high efficiency InAs/GaAs intermediate band solar cell. In Proceedings of the 2017 International Conference on Optical Instruments and Technology: Micro/Nano Photonics: Materials and Devices, Beijing, China, 28–30 October 2017; Volume 10622, pp. 63–74.
42. Kim, D.; Hatch, S.; Wu, J.; Sablon, K.A.; Lam, P.; Jurczak, P.; Tang, M.; Gillin, W.P.; Liu, H. Type-II InAs/GaAsSb Quantum Dot Solar Cells With GaAs Interlayer. *IEEE J. Photovoltaics* **2018**, *8*, 741–745. [CrossRef]


**Disclaimer/Publisher's Note:** The statements, opinions and data contained in all publications are solely those of the individual author(s) and contributor(s) and not of MDPI and/or the editor(s). MDPI and/or the editor(s) disclaim responsibility for any injury to people or property resulting from any ideas, methods, instructions or products referred to in the content.